



Cell division in the shoot apical meristem is a trigger for miR156 decline and vegetative phase transition in *Arabidopsis*

Ying-Juan Cheng^a, Guan-Dong Shang^{a,b}, Zhou-Geng Xu^{a,b}, Sha Yu^a, Lian-Yu Wu^{a,c}, Dong Zhai^{a,b}, Shi-Long Tian^{a,b}, Jian Gao^a, Long Wang^a, and Jia-Wei Wang^{a,c,1}

^aNational Key Laboratory of Plant Molecular Genetics, CAS Center for Excellence in Molecular Plant Sciences (CEMPS), Institute of Plant Physiology and Ecology (SIPPE), Chinese Academy of Sciences (CAS), Shanghai 200032, China; ^bUniversity of Chinese Academy of Sciences, Shanghai 200032, China; and ^cSchool of Life Science and Technology, ShanghaiTech University, Shanghai 201210, China

Edited by Sarah Hake, University of California, Berkeley, CA, and approved October 1, 2021 (received for review August 26, 2021)

What determines the rate at which a multicellular organism matures is a fundamental question in biology. In plants, the decline of miR156 with age serves as an intrinsic, evolutionarily conserved timer for the juvenile-to-adult phase transition. However, the way in which age regulates miR156 abundance is poorly understood. Here, we show that the rate of decline in miR156 is correlated with developmental age rather than chronological age. Mechanistically, we found that cell division in the apical meristem is a trigger for miR156 decline. The transcriptional activity of *MIR156* genes is gradually attenuated by the deposition of the repressive histone mark H3K27me3 along with cell division. Our findings thus provide a plausible explanation of why the maturation program of a multicellular organism is unidirectional and irreversible under normal growth conditions and suggest that cell quiescence is the fountain of youth in plants.

miR156 | age | developmental timing | cell division

Multicellular organisms undergo several developmental transitions during their life cycles (1). Why these transitions are unidirectional and how the rate of these transitions is determined are biological mysteries. Previous studies have shown that both animals and plants utilize a microRNA (miRNA) timer in regulating their developmental transitions. In *Caenorhabditis elegans*, gradual increases in *let-7* and *lin-4* promote the exit from the juvenile phase (2–4). Analogously, the progressive decline in miR156 triggers the appearance of adult traits in plants (5–8). Although the downstream events of these miRNAs have been extensively studied, how age regulates *let-7* and miR156 abundance is poorly understood.

In the aerial parts of flowering plants, all organs including leaves, stems, and flowers originate from a small population of stem cells embedded in the shoot apical meristem (SAM). New leaf primordia are continuously produced in a regular spatial and temporal order on the flanks of the SAM. The gradual changes in morphological and anatomical traits in the successive leaves serve as visible markers of juvenile-to-adult phase transitions (8). It has been shown that overexpression of miR156 prolongs the juvenile phase, whereas blocking the function of miR156 leads to a precociously maturing phenotype (5, 9). Notably, the function of miR156 in the maintenance of juvenility is evolutionarily conserved. For example, elevation of miR156 drastically prolonged juvenile phase in maize, rice, and poplar trees (10–13).

miR156 is transcribed from eight genes in *Arabidopsis thaliana* (14). Earlier reports have shown that the *MIR156A* and *MIR156C* genes play dominant and redundant roles within the gene family in *Arabidopsis* (15). The transcriptional regulation of these two *MIR156* genes has been extensively studied. It has been proposed that sugar promotes vegetative phase change by repressing the expression of *MIR156A/C* (16–18). In addition,

diverse exogenous cues such as temperature (19), phosphate availability (20), and CO₂ concentration (21) can modulate miR156 levels. Furthermore, the transcription factors including FUSCA3, VIVIPAROUS/ABI3-LIKE1 (VAL1)/VAL2, AGL15/18, and MYB33 regulate the abundance of miR156 by directly binding to the promoter regions of *MIR156A/C* (22–25).

Emerging data also suggest that the decrease of miR156 expression is temporally correlated with an increase in the amount of H3K27me3 at the *MIR156A/C* loci in *Arabidopsis* (26). The increase in H3K27me3 is associated with an increase in the amount of POLYCOMB REPRESSIVE COMPLEX2 components, CURLY LEAF and SWINGER (SWN), bound to these genes. Consistently, it has been shown that loss of function of the PRC1 component leads to the up-regulation of *MIR156A/C* expression at the time the levels of miR156 should decline, resulting in an extended juvenile phase and delayed flowering (27). Furthermore, the SWI2/SNF2 chromatin remodeling ATPase BRAHMA and SWN act antagonistically at the nucleosome level to fine-tune the temporal expression of miR156 to regulate vegetative phase change (28).

Based on these previous findings, there are two primary possibilities to explain how miR156 declines with age. One possibility is that silencing of *MIR156* genes occurs in a time-dependent

Significance

Why the developmental transitions of multicellular organisms are unidirectional and how the rate of these transitions is determined are biological mysteries. Earlier reports have shown that both animals and plants utilize microRNA (miRNA) as a timer in regulating their developmental transitions. However, how age temporally regulates the abundance of these miRNAs is poorly understood. In plants, the progressive decline in miR156 triggers the appearance of adult traits. Here, we show that cell division in the apical meristem is a trigger for miR156 decline. The transcriptional decline in *MIR156C* along with cell division in the apical meristem contributes to plant maturation. This simple model explains why the developmental transitions of a plant are unidirectional and inevitable under normal growth conditions.

Author contributions: Y.-J.C. and J.-W.W. designed research; Y.-J.C., S.Y., D.Z., S.-L.T., J.G., and L.W. performed research; L.W. contributed new reagents/analytic tools; Y.-J.C., G.-D.S., Z.-G.X., L.-Y.W., and J.-W.W. analyzed data; and J.-W.W. wrote the paper.

The authors declare no competing interest.

This article is a PNAS Direct Submission.

Published under the PNAS license.

¹To whom correspondence may be addressed. Email: jwwang@sippe.ac.cn.

This article contains supporting information online at <http://www.pnas.org/lookup/suppl/doi:10.1073/pnas.2115667118/-DCSupplemental>.

Published November 8, 2021.

manner, such that chromatin state in a single cell differs over time. Similar scenario has been reported for the repression of *FLC* during vernalization (29). Alternatively, inactivation of *MIR156* genes operates in a cell division-dependent manner, such that chromatin state progresses in a single direction, within cell lineages with each division. Here, we used live imaging and developmental genetics to distinguish between these two possibilities. Our results demonstrate that cell division in the apical meristem is a trigger for miR156 decline. The transcriptional activity of *MIR156C* is gradually attenuated by the deposition of the repressive histone mark H3K27me3 along with cell division. These findings offer fresh mechanistic insights into how miR156 level is regulated in an age-dependent manner and provide a plausible explanation of why the maturation program of a multicellular organism is unidirectional and irreversible under normal growth conditions.

Results

The miR156 Rate of Decline Is Correlated with Developmental Age.

We generated a *MIR156C* reporter using nuclear-localized green fluorescence protein (GFP-N7) as readout. The *MIR156C* genomic fragment used in the reporter construct was able to rescue the precocious phenotype of the *mir156a mir156c* double mutant (*SI Appendix, Fig. S1*), suggesting that this fragment harbors all of the regulatory elements. Time-course analyses of the *MIR156C* reporter showed that green fluorescence was strongest in cotyledons, markedly reduced in the first two true leaves (first and second leaves), and

subsequently decreased in the third and fourth leaf primordia (Fig. 1 *A* and *B*). This expression pattern was consistent with published data (15) and with our qRT-PCR results (Fig. 1 *C* and *D*). Thus, the *MIR156C* reporter mimics the endogenous expression pattern of *MIR156C* and enables us to investigate *MIR156C* expression at cellular resolution.

Plants grow more slowly in short days than in long days. As such, the emergence of the first and second leaf primordium was delayed under short-day conditions (Fig. 1 *A* and *B* and *SI Appendix, Fig. S2A*). If the miR156 level is regulated by chronological age, we would expect that the magnitude of the miR156 decline in the first and second leaf primordium in plants grown in short days would be higher than in plants grown in long days. In contrast to this speculation, the magnitude of the decrease in miR156 and the *MIR156C* reporter in the first and second leaf was comparable between plants grown in long days and short days (Fig. 1 *C* and *D* and *SI Appendix, Table S1*). To confirm this finding, we crossed the *MIR156C* reporter plant with the *kluh/cyp78a5* and *hookless (hls)* mutants, in which the time that elapses between the formation of primordia is shortened (*SI Appendix, Fig. S2A*) (30). The analyses of both mutants gave similar results (*SI Appendix, Fig. S2B*). For example, although the *hls* mutant initiated the third leaf ~2 d earlier than the wild-type, the GFP-N7 fluorescence in the third leaf declined with the same magnitude despite the genetic background (*SI Appendix, Fig. S2 B and C*). Taken together, these results indicate that the miR156 rate of decline is correlated with developmental age rather than chronological age.

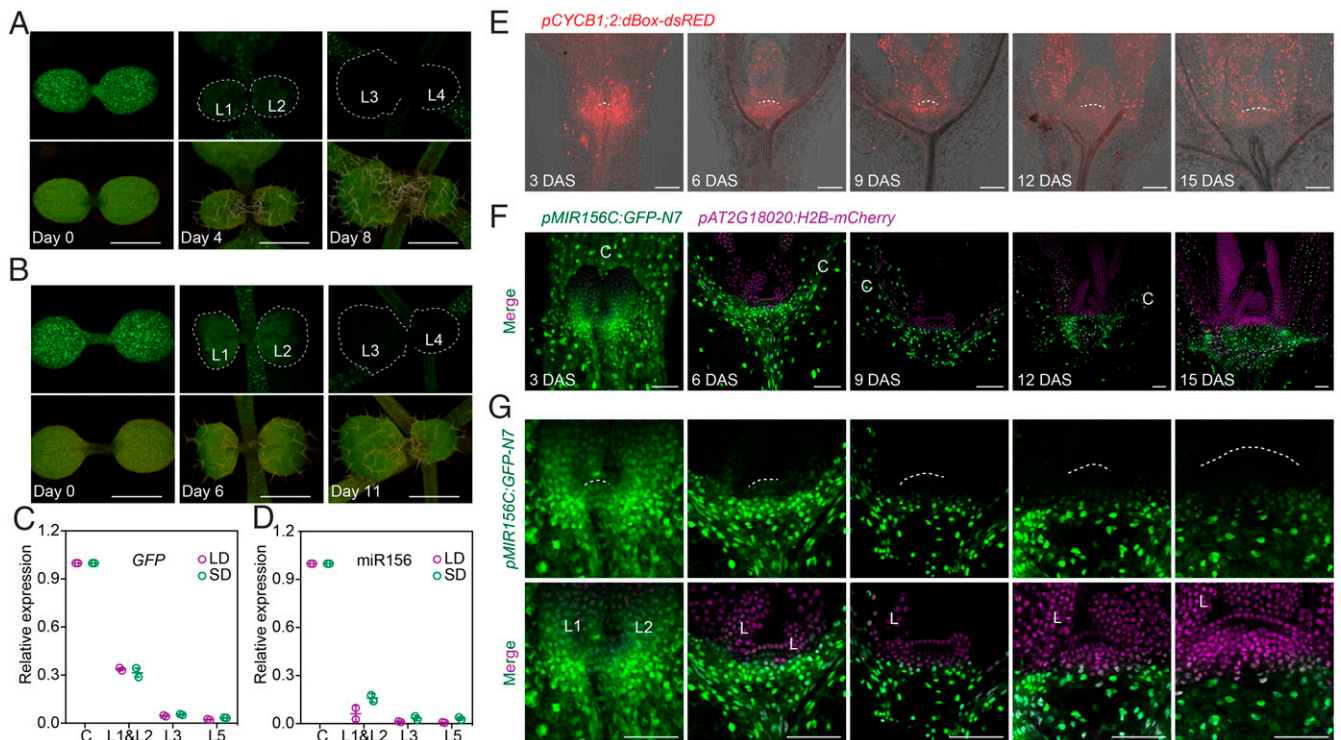


Fig. 1. The rate of *MIR156C* decline is correlated with developmental age rather than chronological age. (A and B) Expression of the *pMIR156C:GFP-N7* reporter in plants grown in long days (A) and short days (B). Dashed lines mark the successive rosette leaves (L1 to L4). GFP-N7 fluorescence of the same plant was examined. The day when the cotyledon was examined is defined as Day 0. (Scale bars, 1.0 mm.) (C and D) Quantification of *GFP-N7* messenger RNAs (mRNAs) (C) and miR156 levels (D) in *pMIR156C:GFP-N7* transgenic plants by qRT-PCR. Plants were grown in long days or short days as in A and B. The days when cotyledon and leaf were harvested are listed in *SI Appendix, Table S1*. C, cotyledon; L1&L2, L3, and L5, the first and second, third, and fifth leaves. Two biological replicates were performed. Error bars indicate the sem. (E) Expression of *pCYCB1;2:dsRED* in the shoot apex. Plants were grown in short days. Dashed lines mark the outline of the SAM. (Scale bars, 50 μm.) (F and G) Expression of the *pMIR156C:GFP-N7 pAT2G18020:H2B-mCherry* dual reporter in the shoot apex. Plants were grown in short days. Homozygous *pMIR156C:GFP-N7* and *pAT2G18020:H2B-mCherry* reporter plants were crossed, and the resulting F₁ plants were examined at different time points as indicated. The zoom-in of the SAM region is shown in G. C, cotyledon; L, rosette leaf. Dashed lines mark the outline of the SAM. (Scale bars, 50 μm.)

The Decline in *MIR156C* and miR156 Is Coupled to Cell Division in the SAM. Because the developmental age of a plant is determined by the rate of lateral organ formation, we postulate that the decline in miR156 is directly coupled with cell division in the SAM. To test this hypothesis, we performed a time-course analysis of the *MIR156C* reporter at cellular resolution in the SAM. The *Arabidopsis* vegetative SAM consists of three distinct functional domains. The central zone (CZ) is located at the summit of the SAM and contains the stem cell population. Stem cell division replenishes the CZ and displaces the daughter cells outward into the peripheral zone (PZ), where new organs are initiated. Beneath the CZ and PZ is the rib zone (RZ), the cells of which are largely mitotically inactive in the juvenile phase but actively divide and contribute to the formation of the stem and vasculature tissues after the floral transition (*SI Appendix, Fig. S3C*) (31–33). Analysis of a cell division reporter (*pCYCB1;2:dBox-dsRED*) revealed active cell division in both the CZ and PZ as well as developing leaf primordia after seed germination, whereas the cells in the RZ were mostly quiescent during the vegetative phase (*Fig. 1E*).

During embryogenesis, apical meristem cells are quiescent (i.e., a reversible state of a cell in which it does not divide but retains cell proliferation potential) until germination. The transcription of *MIR156C* did not decline during embryogenesis (*SI Appendix, Fig. S3 A and B*). To eliminate the possibility that two copies of the *pMIR156C:GFP-N7* transgene were differentially expressed in single cells (34), we crossed *pMIR156C:GFP-N7* with the *pAT2G18020:H2B-mCherry* plant in which the Histone 2B (H2B)-mCherry fusion protein is expressed from the ubiquitous *AT2G18020* promoter. The resulting F₁ plants were used for confocal imaging.

Two days after sowing (DAS), uniform expression of *GFP-N7* was observed in the shoot apex (*SI Appendix, Fig. S3D*). Notably, the *GFP-N7* fluorescent signals in the first and second leaf primordia were comparable to those in the meristematic cells in the PZ (*SI Appendix, Fig. S3D*). Along with cell division in the SAM, we observed an evident decrease in *MIR156C* transcription in the CZ and PZ (*Fig. 1 F and G*), although it remained largely unchanged in the cells at the RZ (*Fig. 1 F and G*). Since the cells in the CZ divide slower than those in the PZ (35), the decline in *GFP-N7* was moderately attenuated in the CZ (*SI Appendix, Fig. S3 E and F*).

To further confirm this result, we generated two miR156 sensor plants in which *GFP-N7* fused with the 3' untranslated region (3' UTR) of *SQUAMOSA PROMOTER BINDING PROTEIN-LIKE3* (*SPL3*) was expressed under control of the *UBQ10* promoter (*pUBQ10:GFP-N7-SPL3 3'UTR*) or *AT2G18020* (*pAT2G18020:GFP-N7-SPL3 3'UTR*). The miR156-targeted site in the *SPL3 3'UTR* enables *GFP-N7* to be regulated by endogenous miR156. Consistent with the above results, the analyses of the miR156 sensors at 10 DAS revealed that miR156 was expressed at low levels in the SAM and developing leaves where cell division is active but accumulated to a high level in the RZ cells which are largely quiescent in the vegetative phase (*SI Appendix, Fig. S4 A and B*). Thus, these data collectively support our hypothesis that the decline in *MIR156C* and miR156 is coupled to cell division in the SAM.

Cell Division Acts as a Proxy for Chronological Age in Regulating *MIR156C* Transcription. To further determine how the miR156 level decreases precisely along with cell division at the postembryonic stage, we examined the *MIR156C* reporter in roots in which the cell division pattern can be easily traced at temporal and spatial resolution. *Arabidopsis* root growth is indeterminate continual, resulting in stem cell populations at the distal end and differentiating cells at the proximal end (*Fig. 2A*). The stem cells at the root tip undergo several divisions before reaching the elongation zone, whereupon cell division no longer

takes place, and the cells begin to differentiate (36, 37). As such, the *pCYCB1;2:dBox-dsRED* reporter was not detectable at the proximal end but continuously expressed at the distal end (*Fig. 2 B and C*). At 2 DAS, the *GFP* signals of *pMIR156C:GFP-N7* were uniformly distributed throughout the root (*Fig. 2D*). Along with cell division, the meristematic cells at the distal end gradually lost their fluorescence, whereas the fluorescence in the cells at the proximal end (i.e., root/shoot junction or collet) slightly decreased before 4 DAS and remained largely unchanged thereafter (*Fig. 2 E and F and SI Appendix, Fig. S5 A and B*). These results were confirmed by qRT-PCR analyses on *GFP-N7* as well as mature miR156 in *pMIR156C:GFP-N7* plants (*Fig. 2G*) and by quantifying *GFP* fluorescence in the miR156 sensor (*SI Appendix, Fig. S4 C and D*). Lateral root primordia arise from pericycle cells of the primary root according to an acropetal sequence. Intriguingly, the lateral root primordia that develop at the proximal end showed higher fluorescence than those at the distal end (*Fig. 2H and SI Appendix, Fig. S6*), regardless of their different timing of initiation. The *GFP* signal intensity in the lateral root primordia at very early developmental stages was similar to that in the surrounding pericycle cells (*Fig. 2I*). Live imaging further revealed that the reporter activity was subsequently decreased along with the development of lateral root primordia (*Fig. 2I and Movies S1 and S2*). Hence, these results are consistent with the aforementioned observations in the SAM and suggest that the original transcriptional activity of *MIR156C* is preserved once the cells become quiescent.

To validate the above conclusion, we grew *MIR156C* reporter lines at low temperature (4 °C) in which the cell division rate is slowed (*Fig. 3A*). In accordance with a decrease in cell division rate at the root meristem zone, the magnitude of the *MIR156C* decline was greatly reduced (*Fig. 3 B and C and SI Appendix, Fig. S8*). Moreover, the application of flavopiridol (FVP), a cyclin-dependent kinase inhibitor that blocks the cell cycle progression at the G1-S and G2-M phases (38), significantly inhibited cell division and interfered with the decline in *MIR156C* transcription at the root tip (*Fig. 3 D–F*). Another cell cycle inhibitor, roscovitine (ROS), had a similar but weaker effect on miR156 expression (*SI Appendix, Fig. S7 A–C*), possibly due to insufficient inhibition of cell division (*SI Appendix, Fig. S8*). Recent studies have revealed that TARGET OF RAPAMYCIN (TOR) kinase acts as a key regulator of SAM and RAM activation by integrating light and metabolic signals (39, 40). Upon treatment with Torin, a TOR inhibitor (41), cell division in the root meristem ceased, accompanied by a defect in the miR156 decline with age (*SI Appendix, Fig. S8 and Fig. 3 G–I*). Taken together, our results indicate that 1) the onset of cell division in meristematic cells is a trigger for the decline in miR156, 2) the cell division in the meristematic cells acts as a proxy for chronological age in regulating *MIR156C* transcription, and 3) the transcriptional activity of *MIR156C* is preserved in the quiescent cells.

Deposition of H3K27me3 Contributes to Cell Division-Dependent Decline of *MIR156C*. To understand the molecular mechanism by which age regulates miR156 transcription, we employed a forward genetics approach by mutagenizing the miR156 sensor plant, *pUBQ10:GFP-N7-SPL3 3'UTR*. In the wild-type background, the *GFP-N7* signals were weak in the first and second leaves but strongly elevated in the third and fourth leaves (*SI Appendix, Fig. S9A*), in agreement with the expression pattern revealed by the *MIR156C* reporter. We identified a mutant (named *16W2*), which showed weak *GFP-N7* expression in the third and fourth leaves (*SI Appendix, Fig. S9 B–D*). Compared to wild-type, the transition from the juvenile-to-adult phase was delayed in *16W2* (*SI Appendix, Fig. S9E*). Fine mapping by sequencing revealed that the mutant phenotype was caused by mutations in two genes (42). The gene on chromosome 2

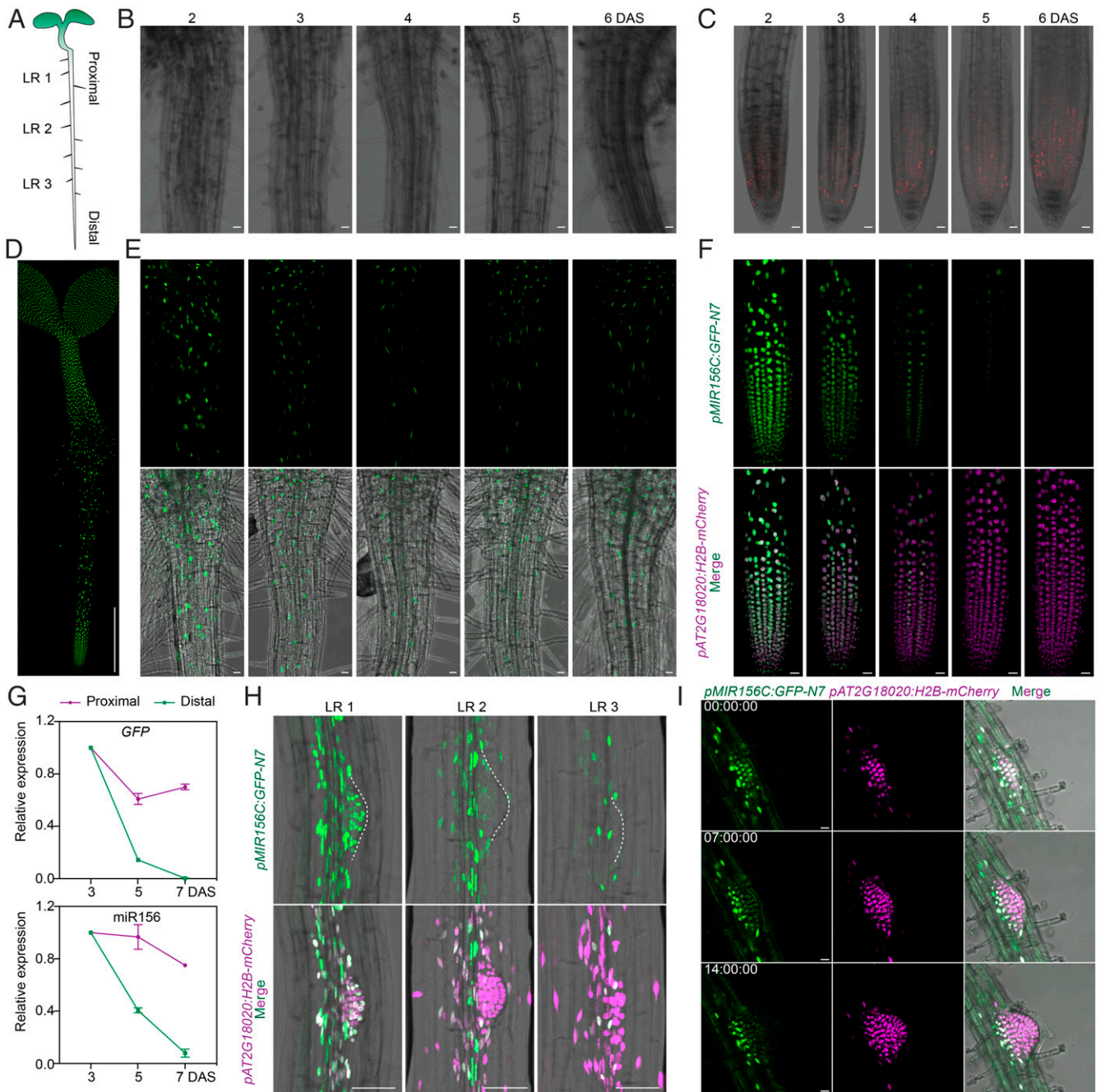


Fig. 2. Cell division is a trigger for *MIR156C* decline. (A) Schematic drawing of a wild-type seedling. The proximal and distal regions of the root are indicated. LR, lateral root. (B and C) Expression of *pCYCB1;2:dsRED* in the proximal (B) and distal (C) regions of the root. Plants were grown on 0.5× MS medium, and fluorescence was examined at five time points from 2 to 6 DAS as indicated. (Scale bars, 20 μm.) (D) Expression of the *pMIR156C:GFP-N7* reporter at 2 DAS. Plants were grown in long days. (Scale bar, 0.5 mm.) (E and F) Expression of the *pMIR156C:GFP-N7 pAT2G18020:H2B-mCherry* dual reporter in the proximal (E) and distal (F) regions of the root. Plants were grown on 0.5× MS medium, and fluorescence was examined at five time points from 2 to 6 DAS as indicated in B and C. (Scale bars, 20 μm.) (G) Quantification of *GFP-N7* mRNAs and miR156 in *pMIR156C:GFP-N7* plants by qRT-PCR. The root proximal and distal regions (~1.5 mm in length) were harvested. Two biological replicates were performed. Error bars show the SEM. (H) Expression of the *pMIR156C:GFP-N7 pAT2G18020:H2B-mCherry* dual reporter during the initiation of lateral root primordia. Three lateral root primordia (LR1 to LR3) from the proximal to distal regions along the primary root (A) were examined at the same time. Dashed lines mark the outline of lateral root primordia. (Scale bars, 50 μm.) (I) Snapshots of the live imaging of the *pMIR156C:GFP-N7 pAT2G18020:H2B-mCherry* dual reporter during the initiation of lateral root primordia. (Scale bars, 20 μm.)

encodes ENHANCED MIRNA ACTIVITY1 (EMA1), an importin beta-like protein that negatively regulates miRNA activity (43), whereas the gene on chromosome 3 encodes HISTONE DEACETYLASE9 (HDA9), an RPD3-type deacetylase that is critical for deacetylation of H3K9 (H3K9ac) and H3K27 (H3K27ac) (SI Appendix, Fig. S9F) (44, 45). Analyses of *ema1*

and *hda9* single mutants indicated that both genes contribute to the mutant phenotype (SI Appendix, Fig. S9 G and H). Because EMA1 acts as a general factor in regulating miRNA activity, we focused on the role of *HDA9* on miR156 expression in the subsequent experiments. Plants with mutations in *POWERDRESS* (*PWR*) and *HIGH EXPRESSION OF*

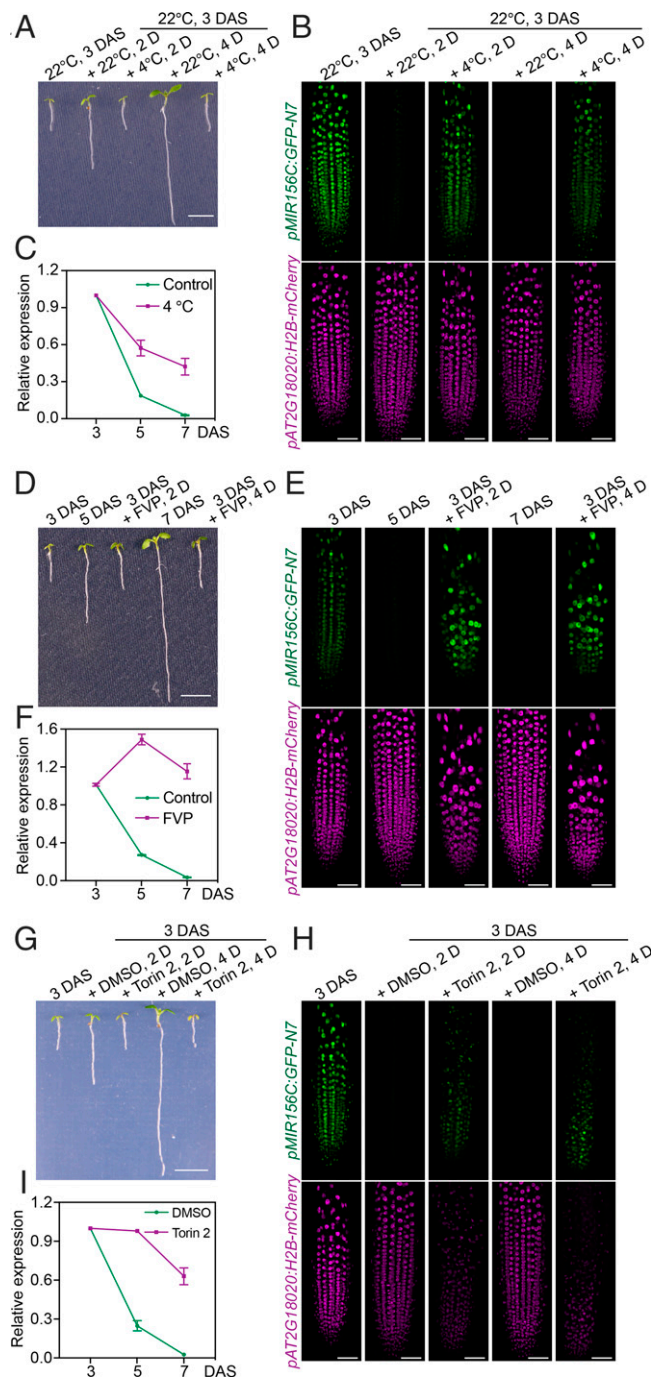


Fig. 3. Inhibition of cell division attenuates the decline of *MIR156C*. (A and B) Low temperature reduces root growth rate (A) and attenuates the decline of *MIR156C* (B). The *pMIR156C:GFP-N7 pAT2G18020:H2B-mCherry* dual reporter seedlings were grown on a vertical 0.5× MS plate for 3 d (3 DAS) and then transferred to 4°C for 2 or 4 d. (Scale bars, 0.5 cm in A and 50 μm in B). (C) Quantification of *GFP-N7* mRNAs in the *pMIR156C:GFP-N7* reporter at root distal regions in response to cold treatment by qRT-PCR. Expression of *GFP-N7* before treatment (3 DAS) was set to 1.0. Plants were treated as described in A. Two biological replicates were performed. Error bars show the SEM. (D and E) FVP inhibits cell division in roots (D) and attenuates the decline in *MIR156C* (E). The *pMIR156C:GFP-N7 pAT2G18020:H2B-mCherry* dual reporter seedlings were grown on a vertical 0.5× MS plate for 3 d (3 DAS) and then treated with 10 μM FVP for 2 or 4 d. (Scale bars, 0.5 cm in D and 50 μm in E). (F) Quantification of *GFP-N7* mRNAs in the *pMIR156C:GFP-N7* reporter at root distal regions in response to FVP treatment by qRT-PCR. The expression level of *GFP-N7* before treatment (3 DAS) was set to 1.0. Plants were treated as described in D. Three biological replicates were

OSMOTICALLY RESPONSIVE GENE15 (HOS15), which encode components in the same histone deacetylase complex with HDA9 (46), exhibited a similar juvenilized phenotype (Fig. 4 A and B). The weak phenotype of *hda9* was likely due to the functional redundancy of the histone deacetylase gene family in *Arabidopsis*. Indeed, an enhancement of the juvenilized phenotype was observed in *hda6 hda7 hda9* triple-mutant plants (Fig. 4A).

H3K27ac is a mark of active chromatin and is negatively correlated with the repressive histone modification marker H3K27me3 in *Arabidopsis* (47). As mentioned in the introduction, emerging data suggest that miR156 expression is positively correlated with H3K27ac and inversely correlated with H3K27me3 at the *MIR156A/C* loci (26). To precisely investigate the role of cell division and histone modifications in regulating miR156 and *MIR156C* expression, we used roots as the experimental system. Compared to the wild-type, the *hda6 hda7 hda9* triple mutant did not have an effect on root growth (SI Appendix, Fig. S10). The decline in *GFP-N7* was attenuated in root tips of the *hda6 hda7 hda9* triple-mutant plants compared to wild-type (Fig. 4C). Consistently, chromatin immunoprecipitation followed by qPCR (ChIP-qPCR) revealed that the H3K27ac levels at *MIR156C* locus were higher in *hda6 hda7 hda9* plants than in wild-type (Fig. 4D).

To determine whether histone modifications are engaged in the cell division-dependent decline in miR156, we examined the temporal-spatial deposition of the H3K27ac and H3K27me3 marks at the *MIR156C* locus by the chromatin immunoprecipitation followed by sequencing (ChIP-seq). To this end, we harvested distal and proximal regions of the roots from wild-type seedlings of different ages. At 3 DAG, the H3K27ac level at the *MIR156C* locus was comparable in the distal and proximal regions. At 7 DAG, the H3K27ac level was greatly reduced in the distal region but remained unaltered in the proximal region (Fig. 4E). A parallel analysis of H3K27me3 levels revealed that the H3K27me3 mark was progressively deposited at the *MIR156C* locus only in the root tip. Notably, H3K27me3 levels at the *MIR156C* locus did not change along with time when cell division in the roots was blocked by FVP treatment (Fig. 4E). Taken together, the above results suggest that the gradual decrease in H3K27ac at the *MIR156C* locus along with cell division is accompanied by their transcriptional shutdown. This epigenetic change in turn facilitates the binding of Polycomb group proteins and the deposition of the repressive histone mark H3K27me3. Consequently, H3K27me3 serves as a transmissible mark, leading to a mitotically stable repression of *MIR156C*.

Discussion

Our results suggest that the transcriptional decline in *MIR156C* along with cell division in the apical meristem contributes to plant maturation. This simple model explains why the decline in miR156 is inevitable. In addition, it provides a plausible explanation to why the root crown and the stem base (trunk) of perennial trees remain juvenile both morphologically and physiologically (48). Moreover, it supports the recent findings that an unexpectedly low number of cell divisions separate apical from axillary meristems (49–51).

performed. Error bars show the SEM. (G and H) Torin 2 inhibits cell division in roots (G) and attenuates the decline in *MIR156C* (H). The *pMIR156C:GFP-N7 pAT2G18020:H2B-mCherry* dual reporter seedlings were grown on a vertical 0.5× MS plate for 3 d (3 DAS) and then treated with Torin 2 for 2 or 4 d. (Scale bars, 0.5 cm in G and 50 μm in H.) (I) Quantification of *GFP-N7* mRNAs in the *pMIR156C:GFP-N7* reporter at root distal regions in response to Torin 2 treatment by qRT-PCR. The expression level of *GFP-N7* before treatment (3 DAS) was set to 1.0. Plants were treated as described in G. Two biological replicates were performed. Error bars show the SEM.

The coupling of cell division in the SAM and miR156 abundance further explains previous observations that both nutrients and temperature can affect plant maturation rate (16–18, 21). It is also interesting to note that growth retardation has recently been identified as part of a timing system to measure prolonged cold treatment during vernalization (52), suggesting that the growth-mediated regulatory mechanism may be widely adopted for plant developmental transitions. Finally, the contribution of HDA9 to division-dependent miR156 decline is reminiscent of

replicative aging mediated by the conserved longevity histone deacetylase Sir2 in yeast (53). Therefore, it will be interesting to see whether such a paradigm is adopted for the temporal regulation of *let-7* or *lin-4* in *C. elegans*.

The adult plants can be rejuvenated under certain conditions. For example, repeated grafting of adult shoot tips onto juvenile rootstocks leads to the regaining of juvenile physiological and molecular characteristics (54–57). Alternatively, rejuvenation can be achieved by severe pruning and in vitro tissue

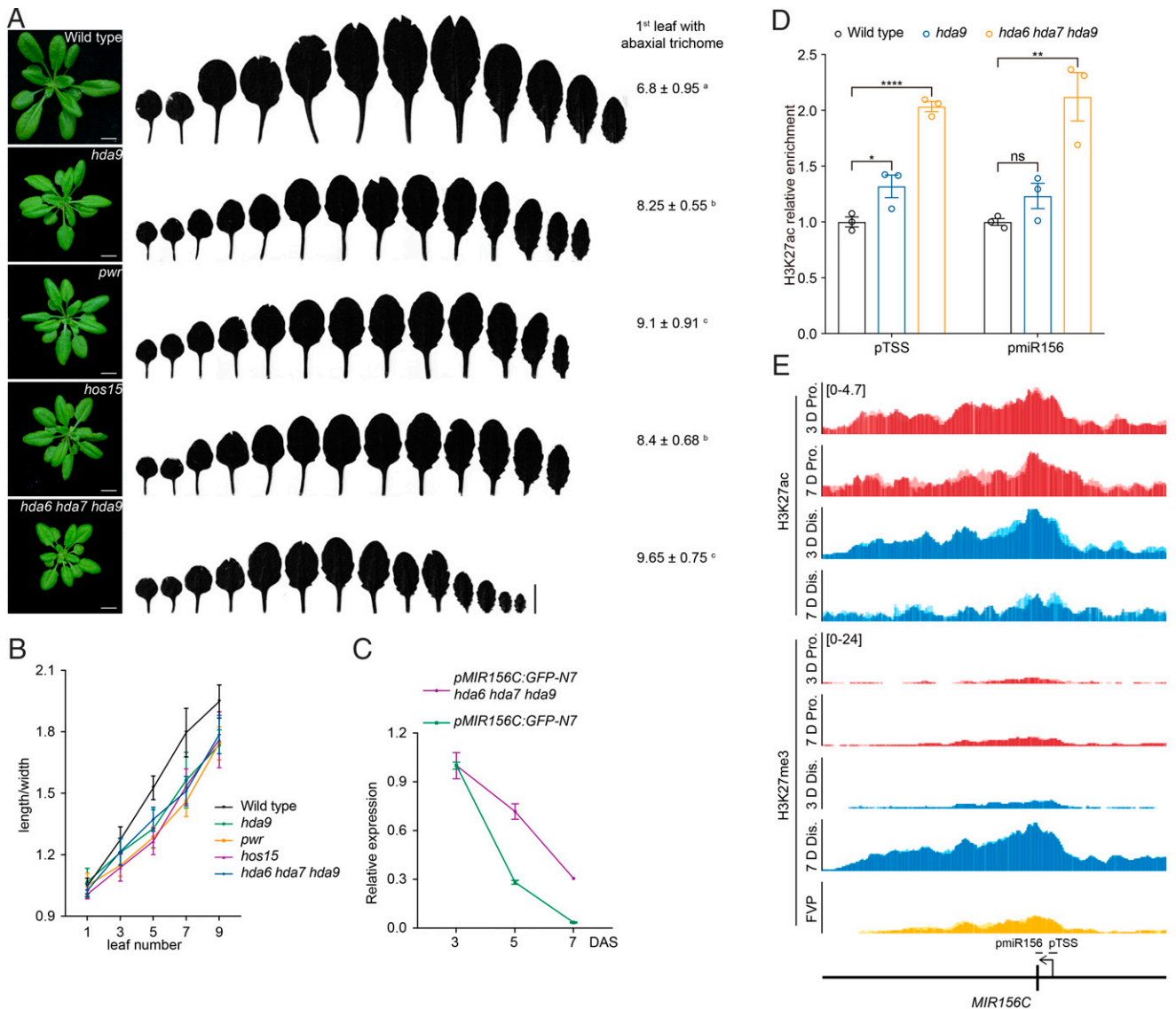


Fig. 4. HDA9 contributes to cell division-dependent decline in *MIR156C*. (A) Plant morphology and quantification of the first leaf with abaxial trichomes. Plants were grown for 28 d in long days. A total 20 plants for each genotype were examined. The data for wild-type were the same as in *SI Appendix, Fig. S1B*. The statistically significant differences are determined by ordinary one-way ANOVA ($P < 0.05$). (Scale bars, 1.0 cm.) (B) Quantification of leaf length/width ratio. Plants were grown in long days. The ratio of the first, third, fifth, seventh, and ninth leaf was examined. A total 10 plants for each genotype were examined. The data for wild-type were the same as in *SI Appendix, Fig. S1C*. Error bars show the SD. (C) Quantification of *GFP-N7* mRNA levels in the distal region of the *pMIR156C:GFP-N7* roots by qRT-PCR. The expression level at 3 DAS is set to 1.0. Two biological replicates were performed. Error bars show the SEM. (D) The level of H3K27ac at the *MIR156C* locus in wild-type, *hda9*, and *hda6 hda7 hda9* mutant. Two regions (pTSS, transcription start site; pmiR156, the stem-loop region of miR156, [E]) were examined. The distal root regions of 5-d-old seedlings were harvested for ChIP-qPCR assays. The level of H3K27ac in wild-type was set to 1.0. Three biological replicates were performed. Error bars show the SEM. One-way ANOVA was performed followed by Dunnett's multiple comparison test, $*P < 0.05$, $**P < 0.01$, $****P < 0.0001$, and ns, not significant. (E) Histone modifications at the *MIR156C* locus. Wild-type seedlings were grown on vertical 0.5× MS plates. The proximal and distal regions are harvested on days 3 and 7 and subjected to ChIP-seq analyses using anti-H3K27ac and anti-H3K27me3 antibodies. For the FVP experiment, wild-type seedlings were grown on vertical 0.5× MS plates for 3 d and treated with 10 μM FVP for 4 d. The distal regions were then harvested. The black vertical line represents the location of the mature miR156 sequence. The TSS is indicated by the arrow. Two biological replicates were shown by dark and light colors, respectively. The values in square brackets represent normalized read counts.

culture (54–57). Intriguingly, previous studies have shown that the level of miR156 is increased during regeneration (58), suggesting that the silencing state at the *MIR156* loci can be reversed upon cell reprogramming. Hence, future work should dissect whether miR156 is reactivated during rejuvenation and how a mitotically stable repression state of *MIR156C* in the adult somatic cells is reset along with regeneration.

Materials and Methods

Plant Materials and Growth Conditions. The *Arabidopsis* plants were grown at 22 °C in growth chambers under long-day (16-h light/8-h dark) or short-day (8-h light/16-h dark) conditions. For the experiments with root tissues, seeds were surface sterilized and kept at 4 °C for 3 d. The seeds were germinated and grown on vertical half-strength (0.5) Murashige and Skoog (MS) agar plates for the indicated time.

The *A. thaliana* ecotype Col-0 was used as wild-type. The *kluhl1cyp78a5* (SM_3_39145) mutant has been described (30). The *hda9* (SALK_007123), *hls* (SALK_136528), *pwr* (SALK_071811), and *hos15* (GABL_785B10) were ordered from Arabidopsis Biological Resource Center (ABRC). The *ema1* (SALK_133577), *hda6* (*axe1-5*), and *hda7* (SALK_002912) mutants were kindly provided by the Yijun Qi (59), Xuelu Wang (60), and Shu-Nong Bai laboratories (61), respectively. The *pCYCB1;2:dsRED* transgenic line was kindly provided by Dr. Hong-Bo Tang. The *mir156a mir156c* mutant was generated by Dr. Jian Gao. The *hda6 hda7 hda9* triple mutants was generated by crossing and PCR-based genotyping. The primers for mutant genotyping are given in *SI Appendix, Table S2*.

Constructs and Generation of Transgenic Plants. The oligonucleotide primers for all constructs are given in *SI Appendix, Table S2*.

To generate *pMIR156C:GFP-N7* reporter, 3.9-kb upstream and 3.1-kb downstream sequences of the stem-loop region of *MIR156C* and coding sequence of *GFP-N7* were PCR amplified. The purified DNA fragments were cloned into the binary vector AA00. To generate the *MIR156C* complementation construct, the *GFP-N7* coding sequence in the *pMIR156C:GFP-N7* construct was replaced by the stem-loop region of *MIR156C*.

For *pAT2G18020:H2B-mCherry* construct, the 2.7-kb upstream regulatory sequence of *AT2G18020* and the coding regions of *H2B* (AT5G22880) and *mCherry* were PCR amplified. The purified DNA fragments were cloned into the binary vector LZ10.

For the miR156 control sensor constructs (*pUBQ10:GFP-N7-NOS* and *pAT2G18020:GFP-N7-NOS*), the *GFP-N7* fragment was cloned into the binary vector JW1078 behind the *UBQ10* promoter or into the binary vector JW805 behind the *AT2G18020* promoter, respectively.

The miR156 sensor constructs (*pUBQ10:GFP-N7-SPL3 3'UTR* and *pAT2G18020:GFP-N7-SPL3 3'UTR*) were generated by replacing *NOS* terminator in control sensors with *SPL3 3'UTR* sequence.

The binary constructs were delivered into *Agrobacterium tumefaciens* strain GV3101 (pMP90) by the freeze–thaw method. Transgenic plants were generated by the floral dipping method (62) and screened with 0.05% glufosinate (Basta) on soil or 40 mg/mL hygromycin on 0.5× MS agar plate.

ChIP-seq and ChIP-qPCR Experiments. ChIP-seq was performed according to previously published protocols with a few modifications (63, 64). For each biological replicate of *Arabidopsis* root ChIP-seq experiments, the distal (~1.5 mm in length) and proximal (~1.5 mm in length) root regions were harvested from ~500 *Arabidopsis* seedlings. Tissues were harvested and grounded into fine powder with liquid nitrogen in 2.0-mL centrifuge tubes using a tissue breaker. The powder was resuspended with Nuclei Isolation Buffer II (0.25 M sucrose, 10 mM Tris-HCl pH 8.0, 10 mM MgCl₂, 1% Triton X-100, 1 mM ethylenediaminetetraacetic acid [EDTA], 5 mM β-mercaptoethanol, 0.4 mM phenylmethylsulfonyl fluoride [PMSF], and protease inhibitor cocktail [Roche, Cat No./ID: 04693132001]) and then filtered through a Falcon 40 μm cell strainer (Corning Falcon, Category No./ID: 352340). After centrifuging, the nuclei pellet was resuspended in 200 μL of micrococcal nuclease (MNase) digestion buffer (50 mM Tris-HCl pH 8.0, 0.2% Triton X-100, 5 mM CaCl₂, 0.5 mM PMSF, and protease inhibitor cocktail), followed by two flash-freezing sequences in liquid nitrogen. The nuclei were then digested with MNase (Thermo Fisher Scientific, Cat No./ID: 88216) at a concentration of 2 U/mL for 15 min at 37 °C. The reaction was terminated by adding 20 μL 100 mM ethylene glycol tetraacetic acid (EGTA). After centrifuging, the supernatant was transferred to a new 1.5-mL centrifuge tube and diluted with 300 μL of dilution buffer (1.55% Triton X-100, 1.67 mM EDTA, 250 mM NaCl, and protease inhibitor cocktail). The resultant chromatin extract was incubated with 1.5 μL of anti-H3K27me3 (Merck, Cat No./ID: 07449) or anti-H3K27ac antibody (Merck, Cat No./ID:

07360) at 4 °C overnight with rotation. The immunoprecipitated DNAs were incubated with either protein G Dynabeads (Thermo Fisher Scientific, Cat No./ID: 10004D) or protein A Dynabeads (Thermo Fisher Scientific, Cat No./ID: 10002D). The ChIPed DNAs were treated with Proteinase K (Sigma-Aldrich, Cat No./ID: 03115828001) and purified with the PCR Purification Kit (Qiagen, Cat No./ID: 28006). Either 1 ng input or ChIPed DNAs were used for ChIP-seq library preparation according to the user manual of SMARTer ThruPLEX DNA-Seq Kit (Clontech, Cat No./ID: R400674). For each experiment, two biological replicates were performed.

ChIP-qPCR was performed with input or ChIPed DNAs as template using TB Green Premix Ex Taq II according to user's manual (Takara, Cat No./ID: RR820B). The “% of input” value represents the enrichment of H3K27ac modification on specific region and then normalized against wild-type. The oligonucleotide primers for qPCR are given in *SI Appendix, Table S2*.

Expression Analyses. For each biological replicate, we harvested cotyledons or developing leaf primordia (~1.0 mm in length) from ~20 *Arabidopsis* plants, the distal (~1.5 mm in length) and proximal (~1.5 mm in length) root tissues from ~200 *Arabidopsis* seedlings.

Total RNAs were extracted with the miRNeasy Micro Kit (Qiagen, Cat No./ID: 217084). Either 250 ng or 1 μg RNA was treated with DNase I (1.0 unit/μL; Thermo Fisher Scientific, Cat No./ID: EN0521), and complementary DNAs (cDNAs) were synthesized with the RevertAid First Strand cDNA Synthesis Kit (Thermo Fisher Scientific, Cat No./ID: K1622) with oligo (dT) primer and miR156 specific reverse transcription (RT) primer (65). The relative gene expression levels were calculated from 2^{-ΔΔCt} values and normalized against *UBC9* (AT4G27960, for *Arabidopsis* root experiments) (66), *AT4G26410* (for *Arabidopsis* leaf experiments) (67), and *UBQ10* (AT4G05320, for *Arabidopsis* embryo experiments) (68). These reference genes were selected based on their expression stabilities across examined samples. The oligonucleotide primers for all genes are given in *SI Appendix, Table S2*.

Plant Treatment. For cold treatment, seedlings were grown on 0.5× MS agar plates for 3 d and shifted to a 4 °C growth chamber. For chemical treatment, 3-d-old seedlings grown on 0.5× MS agar plates were transferred to the 0.5× MS agar plates supplemented with 10 μM FVP hydrochloride (FVP-HCl, MCE, Cat No./ID: HY-10006), 2.0 or 5.0 μM ROS (Millipore-Sigma, Cat No./ID: 557364), 25 μM Torin 2 (MedChemExpress, Cat No./ID: HY-13002), or Dimethyl sulfoxide (DMSO) (mock). The seedlings were grown for another 2 or 4 d before harvest.

EdU Labeling. For the EdU labeling experiment, 3-d-old seedlings were transferred to a small dish containing 0.5× MS liquid media supplemented with 15 mM sucrose and 2.5 μM EdU. After incubating for 1 h at room temperature, seedlings were washed three times with 0.5× MS liquid media and then transferred to the 0.5× MS agar plates supplemented with 8 μM FVP-HCl, 5.0 μM ROS, 25 μM Torin 2, or DMSO, respectively. After 2 or 4 d, seedlings were collected and immediately placed in the vials with ice-cold phosphate-buffered saline (PBS) containing 2.5% paraformaldehyde (PFA, pH 7.0). The samples were infiltrated by vacuum for 30 min and stored at 4 °C overnight. The remaining procedures were performed using Click-IT Plus EdU Imaging Kit (Thermo Fisher Scientific, Cat No./ID: C10637) according to user's manual.

Tissue Embedding and Sectioning. Tissue embedding and sectioning were performed as previously described (68). Briefly, samples were collected and immediately placed in the vials with ice-cold PBS containing 2.5% PFA (pH 7.0). The samples were infiltrated by vacuum for 30 min and stored at 4 °C overnight. Tissues were then washed with sucrose gradient PBS–PFA solution, embedded with 7% low-melting agarose, and sliced with a Lecia Sliding Microtome 1200S at the thickness of 30 to 50 μm.

Microscopy. To observe GFP-N7 fluorescence of cotyledons and leaves, plants were examined and photographed under a stereo microscope (Nikon, SMZ18). For each experiment, all images were acquired using identical settings.

For confocal imaging of *pMIR156C:GFP-N7* line, *pMIR156C:GFP-N7* plant was crossed to *pAT2G18020:H2B-mCherry* plant, and the resultant F1 plants were examined. For confocal imaging of *pCYCB1;2:dsRED*, miR156 sensor, and control sensor, the corresponding homozygous transgenic lines were examined. For EdU imaging, the homozygous *pAT2G18020:H2B-mCherry* plants were used. Images were taken with an inverted Leica TSC SP8 STED 3× confocal microscopic system (Leica, Germany) or OLYMPUS FV3000 confocal microscopic system (Olympus, Japan) with GFP and Alexa Fluor 488 excitation at 488 nm and emission at 498 to 540 nm, mCherry excitation at 561 nm and emission at 590 to 650 nm, and dsRED excitation at 561 nm and emission at 570 to 600 nm. For each experiment, all images were acquired using identical

settings. Z-stack images were taken except the tissue sections of the shoot apices for *pMIR156C::GFP-N7*.

To measure the fluorescent intensities of miR156 sensor and control sensor in roots, approximately the same thickness of tissue at each position was selected and processed using Fiji by applying maximum intensity Z-projection. The root regions on each processed images were selected, and GFP mean intensity was measured using ImageJ.

For live imaging, seedlings were grown on a MS agar plate supplemented with 2% (weight/volume) sucrose in a 35-mm cell imaging dish (Eppendorf, Cat No./ID: 0030740017) for 6 d before imaging. Images were taken every 20 min using the setting for detecting GFP and mCherry as described above.

Image Analysis. Images were processed using Fiji (69). Briefly, root confocal images were processed by applying maximum intensity Z-projection on the outer two cell layers (epidermis and cortex). Fluorescent intensities in the three-dimensional volume was acquired using Imaris image analysis software (Bitplane). The cells of outer two cell layers (epidermis and cortex) of the meristematic zone for each root were selected for analyses. Nuclei were identified based on mCherry signals, and the same arguments were applied to all images. To measure the fluorescent intensities of the L1 layer in the SAM, the Plot Profile function in Fiji was used.

Mutant Screening and Mapping by Sequencing. In brief, the M₂ ethyl methanesulfonate (EMS)-mutagenized miR156 sensor (*pUBQ10::GFP-N7-SPL3 3' UTR*) seeds were sown on soil and grown in long days. The third and fourth leaves were examined by fluorescence stereo microscope (Nikon, SMZ18). The plants with low fluorescence in the third and fourth leaves were labeled as candidate mutants. The mutant phenotype was confirmed in the M3 generation.

We adopted a strategy similar to SHOREmap (42) and MutMap (70) methods for physical mapping. The candidate mutant named 16W2 was backcrossed to *pUBQ10::GFP-N7-SPL3 3' UTR* once and selfed. Two plant pools were generated from the resultant F2 progenies: the “wild-type” pool with high fluorescence in the third and fourth leaves and normal phenotype and the “mutant” pool with low fluorescence in the third and fourth leaves and prolonged juvenile phase phenotype. The plant tissues for each pool were evenly pooled, and genomic DNAs were prepared for the whole genome resequencing.

To retrieve the single-nucleotide polymorphisms (SNPs) of each sample for downstream analysis, we mapped all the reads to the *Arabidopsis* reference genome (TAIR10) with BWA-MEM (71). Duplicated reads were identified and removed with SAMBAMBA (72). HaplotypeCaller from GATK (73) was then used to call variants. The SNPs were filtered based on the following threshold, $QD < 2.0 \parallel FS > 60.0 \parallel MQ < 40.0 \parallel MQRankSum < -12.5 \parallel ReadPosRankSum$

< -8.0 . The allele frequencies in both pools were calculated as the number of reads supporting the mutant allele divided by the number of reads at a SNP position and visualized along the chromosomes to identify mapping intervals as previously described in R statistical environment (74).

Analysis of ChIP-Seq Data. The ChIP-seq libraries were sequenced on Illumina HiSeq-PE150. For each library, raw.fastq was trimmed by fastp version 0.20.0 with default parameters. After trimming, FastQC version 0.11.7 (<https://www.bioinformatics.babraham.ac.uk/projects/fastqc/>) and MultiQC version 1.6 were performed as quality control to obtain clean fq files (75).

Reads were aligned to the *Arabidopsis* (TAIR10) genomes using Bowtie2 version 2.3.4.3 (76, 77). The resulting SAM files were converted to BAM format, sorted, and indexed using Samtools version 1.9 (78). Two biological replicates were merged using Samtools version 1.9. The sorted BAM files were processed to remove duplicated and organellar reads using bedtools version 2.25.0 (72, 79). To normalize and visualize individual and merged replicate datasets, the BAM files were converted to bigwig using bamCoverage provided by deepTools version 3.1.2 with a bin size of 10 bp and normalized by Bin Per Million mapped reads (80). Correlation coefficients between samples were calculated, and heatmap was generated by deepTools version 3.1.2 using spearman method (*SI Appendix, Fig. S11*).

Data Availability. The ChIP-seq data have been deposited in Beijing Institute of Genomics Data Center (<http://bigd.big.ac.cn>) (BioProject accession No. PRJCA003865). All other study data are included in the article and/or supporting information.

ACKNOWLEDGMENTS. We thank Arabidopsis Biological Resource Center, Dr. Yijun Qi (Tsinghua University, China), Dr. Xuelu Wang (Henan University, China), Dr. Shu-Nong Bai (Peking University, China), and Dr. Hong-Bo Tang (CEMPS/SIPPE) for seeds; Dr. Ling-Zi Li (CEMPS/SIPPE) for plasmid; Dr. Yan Xiong (Fujian Agriculture and Forestry University, China) for assistance and advice on Torin 2 treatment; Yun-Xiao He, Shui-Ning Yin, Dr. Wen-Juan Cai, and Xiao-Shu Gao at Core Facility Center of CEMPS/SIPPE, CAS and Dr. Heng Lian for technical support on confocal microscope; and members in the J.-W.W. laboratory for discussion and comments on the manuscript. This work was supported by the grants from the National Key Research & Development Program (2016YFA0500800) to J.-W.W., National Natural Science Foundation of China (31788103; 31761133010; 31525004; and 31721001) to J.-W.W., Strategic Priority Research Program of the Chinese Academy of Sciences (XDB27030101) to J.-W.W., Science and Technology Commission of Shanghai Municipality (18JC1415000) to J.-W.W., and Shanghai Postdoctoral Excellence Program (2019029) to Y.-J.C.

1. I. Bäurle, C. Dean, The timing of developmental transitions in plants. *Cell* **125**, 655–664 (2006).
2. V. Ambros, MicroRNAs and developmental timing. *Curr. Opin. Genet. Dev.* **21**, 511–517 (2011).
3. E. G. Moss, Heterochronic genes and the nature of developmental time. *Curr. Biol.* **17**, R425–R434 (2007).
4. A. E. Pasquinelli, G. Ruvkun, Control of developmental timing by microRNAs and their targets. *Annu. Rev. Cell Dev. Biol.* **18**, 495–513 (2002).
5. G. Wu, R. S. Poethig, Temporal regulation of shoot development in *Arabidopsis thaliana* by miR156 and its target SPL3. *Development* **133**, 3539–3547 (2006).
6. P. Huijser, M. Schmid, The control of developmental phase transitions in plants. *Development* **138**, 4117–4129 (2011).
7. R. S. Poethig, Small RNAs and developmental timing in plants. *Curr. Opin. Genet. Dev.* **19**, 374–378 (2009).
8. S. Yu, H. Lian, J. W. Wang, Plant developmental transitions: The role of microRNAs and sugars. *Curr. Opin. Plant Biol.* **27**, 1–7 (2015).
9. J. W. Wang, B. Czech, D. Weigel, miR156-regulated SPL transcription factors define an endogenous flowering pathway in *Arabidopsis thaliana*. *Cell* **138**, 738–749 (2009).
10. J. W. Wang et al., miRNA control of vegetative phase change in trees. *PLoS Genet.* **7**, e1002012 (2011).
11. Y. Wang et al., miR156 regulates anthocyanin biosynthesis through SPL targets and other microRNAs in poplar. *Hortic. Res.* **7**, 118 (2020).
12. G. Chuck, A. M. Cigan, K. Saetern, S. Hake, The heterochronic maize mutant *Corngrass1* results from overexpression of a tandem microRNA. *Nat. Genet.* **39**, 544–549 (2007).
13. K. Xie et al., Gradual increase of miR156 regulates temporal expression changes of numerous genes during leaf development in rice. *Plant Physiol.* **158**, 1382–1394 (2012).
14. B. J. Reinhart, E. G. Weinstein, M. W. Rhoades, B. Bartel, D. P. Bartel, MicroRNAs in plants. *Genes Dev.* **16**, 1616–1626 (2002).
15. J. He et al., Threshold-dependent repression of SPL gene expression by miR156/miR157 controls vegetative phase change in *Arabidopsis thaliana*. *PLoS Genet.* **14**, e1007337 (2018).
16. S. Yu et al., Sugar is an endogenous cue for juvenile-to-adult phase transition in plants. *eLife* **2**, e00269 (2013).
17. L. Yang, M. Xu, Y. Koo, J. He, R. S. Poethig, Sugar promotes vegetative phase change in *Arabidopsis thaliana* by repressing the expression of *MIR156A* and *MIR156C*. *eLife* **2**, e00260 (2013).
18. V. Wahl et al., Regulation of flowering by trehalose-6-phosphate signaling in *Arabidopsis thaliana*. *Science* **339**, 704–707 (2013).
19. H. Lee et al., Genetic framework for flowering-time regulation by ambient temperature-responsive miRNAs in *Arabidopsis*. *Nucleic Acids Res.* **38**, 3081–3093 (2010).
20. L. C. Hsieh et al., Uncovering small RNA-mediated responses to phosphate deficiency in *Arabidopsis* by deep sequencing. *Plant Physiol.* **151**, 2120–2132 (2009).
21. P. May et al., The effects of carbon dioxide and temperature on microRNA expression in *Arabidopsis* development. *Nat. Commun.* **4**, 2145 (2013).
22. C. Guo et al., Repression of miR156 by miR159 regulates the timing of the juvenile-to-adult transition in *Arabidopsis*. *Plant Cell* **29**, 1293–1304 (2017).
23. F. Wang, S. E. Perry, Identification of direct targets of FUSCA3, a key regulator of *Arabidopsis* seed development. *Plant Physiol.* **161**, 1251–1264 (2013).
24. P. Serivichyaswat et al., Expression of the floral repressor miRNA156 is positively regulated by the AGAMOUS-like proteins AGL15 and AGL18. *Mol. Cells* **38**, 259–266 (2015).
25. J. P. Fouracre, J. He, V. J. Chen, S. Sidoli, R. S. Poethig, VAL genes regulate vegetative phase change via miR156-dependent and independent mechanisms. *PLoS Genet.* **17**, e1009626 (2021).
26. M. Xu, T. Hu, M. R. Smith, R. S. Poethig, Epigenetic regulation of vegetative phase change in *Arabidopsis*. *Plant Cell* **28**, 28–41 (2016).
27. S. Picó, M. I. Ortiz-Marchena, W. Merini, M. Calonje, Deciphering the role of POLY-COMB REPRESSIVE COMPLEX1 variants in regulating the acquisition of flowering competence in *Arabidopsis*. *Plant Physiol.* **168**, 1286–1297 (2015).
28. Y. Xu et al., Regulation of vegetative phase change by SWI2/SNF2 chromatin remodeling ATPase BRAHMA. *Plant Physiol.* **172**, 2416–2428 (2016).
29. A. Angel, J. Song, C. Dean, M. Howard, A Polycomb-based switch underlying quantitative epigenetic memory. *Nature* **476**, 105–108 (2011).
30. J. W. Wang, R. Schwab, B. Czech, E. Mica, D. Weigel, Dual effects of miR156-targeted SPL genes and CYP78A5/KLUH on plastochron length and organ size in *Arabidopsis thaliana*. *Plant Cell* **20**, 1231–1243 (2008).

31. A. L. Holt, J. M. van Haperen, E. P. Groot, T. Laux, Signaling in shoot and flower meristems of *Arabidopsis thaliana*. *Curr. Opin. Plant Biol.* **17**, 96–102 (2014).
32. C. Gaillochet, G. Daum, J. U. Lohmann, O cell, where art thou? The mechanisms of shoot meristem patterning. *Curr. Opin. Plant Biol.* **23**, 91–97 (2015).
33. C. M. Ha, J. H. Jun, J. C. Fletcher, Shoot apical meristem form and function. *Curr. Top. Dev. Biol.* **91**, 103–140 (2010).
34. S. Bery, M. Hartley, T. S. Olsson, C. Dean, M. Howard, Local chromatin environment of a Polycomb target gene instructs its own epigenetic inheritance. *eLife* **4**, e07205 (2015).
35. A. R. Jones *et al.*, Cell-size dependent progression of the cell cycle creates homeostasis and flexibility of plant cell size. *Nat. Commun.* **8**, 15060 (2017).
36. J. J. Petricka, C. M. Winter, P. N. Benfey, Control of *Arabidopsis* root development. *Annu. Rev. Plant Biol.* **63**, 563–590 (2012).
37. H. Motte, S. Vanneste, T. Beeckman, Molecular and environmental regulation of root development. *Annu. Rev. Plant Biol.* **70**, 465–488 (2019).
38. K. Vermeulen, D. R. Van Bockstaele, Z. N. Berneman, The cell cycle: A review of regulation, deregulation and therapeutic targets in cancer. *Cell Prolif.* **36**, 131–149 (2003).
39. A. Pfeiffer *et al.*, Integration of light and metabolic signals for stem cell activation at the shoot apical meristem. *eLife* **5**, e17023 (2016).
40. X. Li *et al.*, Differential TOR activation and cell proliferation in *Arabidopsis* root and shoot apices. *Proc. Natl. Acad. Sci. U.S.A.* **114**, 2765–2770 (2017).
41. Y. Xiong *et al.*, Glucose-TOR signalling reprograms the transcriptome and activates meristems. *Nature* **496**, 181–186 (2013).
42. K. Schneeberger *et al.*, SHOREmap: Simultaneous mapping and mutation identification by deep sequencing. *Nat. Methods* **6**, 550–551 (2009).
43. W. Wang *et al.*, An importin β protein negatively regulates microRNA activity in *Arabidopsis*. *Plant Cell* **23**, 3565–3576 (2011).
44. X. Chen *et al.*, POWERDRESS interacts with HISTONE DEACETYLASE 9 to promote aging in *Arabidopsis*. *eLife* **5**, e17214 (2016).
45. Y. J. Kim *et al.*, POWERDRESS and HDA9 interact and promote histone H3 deacetylation at specific genomic sites in *Arabidopsis*. *Proc. Natl. Acad. Sci. U.S.A.* **113**, 14858–14863 (2016).
46. K. S. Mayer *et al.*, HDA9-PWR-HOS15 is a core histone deacetylase complex regulating transcription and development. *Plant Physiol.* **180**, 342–355 (2019).
47. C. Liu, F. Lu, X. Cui, X. Cao, Histone methylation in higher plants. *Annu. Rev. Plant Biol.* **61**, 395–420 (2010).
48. I. Wendling, S. J. Trueman, A. Xavier, Maturation and related aspects in clonal forestry—Part I: Concepts, regulation and consequences of phase change. *New For.* **45**, 449–471 (2014).
49. E. Schmid-Siegert *et al.*, Low number of fixed somatic mutations in a long-lived oak tree. *Nat. Plants* **3**, 926–929 (2017).
50. A. Burian, P. Barbier de Reuille, C. Kuhlemeier, Patterns of stem cell divisions contribute to plant longevity. *Curr. Biol.* **26**, 1385–1394 (2016).
51. J. M. Watson *et al.*, Germline replications and somatic mutation accumulation are independent of vegetative life span in *Arabidopsis*. *Proc. Natl. Acad. Sci. U.S.A.* **113**, 12226–12231 (2016).
52. Y. Zhao, R. L. Antoniou-Kourounioti, G. Calder, C. Dean, M. Howard, Temperature-dependent growth contributes to long-term cold sensing. *Nature* **583**, 825–829 (2020).
53. M. R. Gartenberg, J. S. Smith, The nuts and bolts of transcriptionally silent chromatin in *Saccharomyces cerevisiae*. *Genetics* **203**, 1563–1599 (2016).
54. M. C. Bon, O. Monteuis, Rejuvenation of a 100-year-old *Sequoiadendron giganteum* through *in vitro* meristem culture. II. Biochemical arguments. *Physiol. Plant.* **81**, 116–120 (1991).
55. L. C. Huang *et al.*, Rejuvenation of *Sequoia sempervirens* by repeated grafting of shoot tips onto juvenile rootstocks *in vitro*: Model for phase reversal of trees. *Plant Physiol.* **98**, 166–173 (1992).
56. M. S. Greenwood, Rejuvenation of forest trees. *J. Plant Growth Regul.* **6**, 1–12 (1987).
57. T. L. Davenport, Pruning strategies to maximize tropical mango production from the time of planting to restoration of old orchards. *HortScience* **41**, 544–548 (2006).
58. Y. C. Luo *et al.*, Rice embryogenic calli express a unique set of microRNAs, suggesting regulatory roles of microRNAs in plant post-embryonic development. *FEBS Lett.* **580**, 5111–5116 (2006).
59. Y. Cui, X. Fang, Y. Qi, TRANSPORTIN1 promotes the association of MicroRNA with ARGONAUTE1 in *Arabidopsis*. *Plant Cell* **28**, 2576–2585 (2016).
60. Y. Hao, H. Wang, S. Qiao, L. Leng, X. Wang, Histone deacetylase HDA6 enhances brassinosteroid signaling by inhibiting the BIN2 kinase. *Proc. Natl. Acad. Sci. U.S.A.* **113**, 10418–10423 (2016).
61. C. R. Xu *et al.*, Histone acetylation affects expression of cellular patterning genes in the *Arabidopsis* root epidermis. *Proc. Natl. Acad. Sci. U.S.A.* **102**, 14469–14474 (2005).
62. S. J. Clough, A. F. Bent, Floral dip: A simplified method for *Agrobacterium*-mediated transformation of *Arabidopsis thaliana*. *Plant J.* **16**, 735–743 (1998).
63. G. D. Gilfillan *et al.*, Limitations and possibilities of low cell number ChIP-seq. *BMC Genomics* **13**, 645 (2012).
64. S. Cortijo, V. Charoensawan, F. Roudier, P. A. Wigge, Chromatin immunoprecipitation sequencing (ChIP-Seq) for transcription factors and chromatin factors in *Arabidopsis thaliana* roots: From material collection to data analysis. *Methods Mol. Biol.* **1761**, 231–248 (2018).
65. E. Varkonyi-Gasic, R. Wu, M. Wood, E. F. Walton, R. P. Hellens, Protocol: A highly sensitive RT-PCR method for detection and quantification of microRNAs. *Plant Methods* **3**, 12 (2007).
66. H. Wang *et al.*, Reference genes for normalizing transcription in diploid and tetraploid *Arabidopsis*. *Sci. Rep.* **4**, 6781 (2014).
67. T. Czechowski, M. Stitt, T. Altmann, M. K. Udvardi, W. R. Scheible, Genome-wide identification and testing of superior reference genes for transcript normalization in *Arabidopsis*. *Plant Physiol.* **139**, 5–17 (2005).
68. F. X. Wang *et al.*, Chromatin accessibility dynamics and a hierarchical transcriptional regulatory network structure for plant somatic embryogenesis. *Dev. Cell* **54**, 742–757.e8 (2020).
69. J. Schindelin *et al.*, Fiji: An open-source platform for biological-image analysis. *Nat. Methods* **9**, 676–682 (2012).
70. H. Takagi *et al.*, MutMap accelerates breeding of a salt-tolerant rice cultivar. *Nat. Biotechnol.* **33**, 445–449 (2015).
71. H. Li, R. Durbin, Fast and accurate long-read alignment with Burrows–Wheeler transform. *Bioinformatics* **26**, 589–595 (2010).
72. A. Tarasov, A. J. Vilella, E. Cuppen, I. J. Nijman, P. Prins, Sambamba: Fast processing of NGS alignment formats. *Bioinformatics* **31**, 2032–2034 (2015).
73. R. F. McCormick, S. K. Truong, J. E. Mullet, RIG: Recalibration and interrelation of genomic sequence data with the GATK. *G3 (Bethesda)* **5**, 655–665 (2015).
74. R. C. Team, R: A Language and Environment for Statistical Computing. R Foundation for Statistical Computing, Vienna, Austria. <https://www.R-project.org/> (Accessed 26 October 2021).
75. P. Ewels, M. Magnusson, S. Lundin, M. Källér, MultiQC: Summarize analysis results for multiple tools and samples in a single report. *Bioinformatics* **32**, 3047–3048 (2016).
76. B. Langmead, S. L. Salzberg, Fast gapped-read alignment with Bowtie 2. *Nat. Methods* **9**, 357–359 (2012).
77. D. Kim, B. Langmead, S. L. Salzberg, HISAT: A fast spliced aligner with low memory requirements. *Nat. Methods* **12**, 357–360 (2015).
78. H. Li *et al.*, 1000 Genome Project Data Processing Subgroup, The sequence alignment/map format and SAMtools. *Bioinformatics* **25**, 2078–2079 (2009).
79. A. R. Quinlan, I. M. Hall, BEDTools: A flexible suite of utilities for comparing genomic features. *Bioinformatics* **26**, 841–842 (2010).
80. F. Ramirez, F. Dündar, S. Diehl, B. A. Grüning, T. Manke, deepTools: A flexible platform for exploring deep-sequencing data. *Nucleic Acids Res.* **42**, W187–W191 (2014).